AIAA 2004-4060

Analytical and CFD Approximations for Tapered Slab Rocket Motors

O. C. Sams, IV, J. Majdalani and G. A. Flandro
Advanced Theoretical Research Center
University of Tennessee Space Institute
Tullahoma, TN 37388

Propulsion Conference and Exhibit
11–14 July 2004
Fort Lauderdale, FL

Analytical and CFD Approximations for
Tapered Slab Rocket Motors

Oliver C. Sams IV,* Joseph Majdalani,† and Gary A. Flandro‡
University of Tennessee Space Institute, Tullahoma, TN 37388

  Internal flowfield modeling is a requisite for obtaining critical parameters for the design and fabrication of modern solid rocket motors. In this work, the analytical formulation of internal flowfields particular to solid rocket motors with tapered sidewalls is pursued. The analysis employs the vorticity-stream function approach to treat this problem assuming steady, incompressible, inviscid, isothermal and non-reactive flow conditions. The resulting solution is rotational and inviscid following the analyses presented by Culick for a cylindrical solid rocket motor. In an extension to Culick's classic work, Clayton has recently managed to incorporate the effect of tapered walls. Here, a similar approach to that of Clayton will be applied to a slab motor in which the chamber will be modeled as a rectangular channel with porous, tapered sidewalls. The solutions will be shown to be reducible, at leading order, to Taylor's inviscid profile in a channel. The analysis also captures the generation of vorticity at the surface of the propellant and its transport along the streamlines due to axial pressure gradients. It is from the axial pressure gradients that the proper form of the vorticity is ascertained. The method of regular perturbations is used to solve the nonlinear vorticity equation that prescribes the mean flow motion in tapered geometry. Subsequently, numerical results provided by FLUENT$^{\text{TM}}$ and an additional analytical approach (variation of parameters) are used to gain confidence in the analytical approximations obtained from the perturbation method. To further understand the effects of the taper on flow conditions, comparisons of total pressure and velocity profiles in tapered and non-tapered chambers are entertained.

Nomenclature

F = momentum thrust
h_0 = slab motor half-height
L_0 = motor length (slab and cylindrical motors)
$\bar{p}$ = dimensional pressure
p = normalized pressure, $\bar{p}/\rho V_b^2$
$\bar{u}$ = dimensional velocity components, $(\bar{u}_x, \bar{u}_y)$
u = normalized velocity, $\bar{u}/V_b$
V_b = injection velocity at propellant surface
w_0 = slab motor width
$\bar{x}$ = dimensional axial coordinate
x = normalized axial coordinate, $\bar{x}/h_0$
$\bar{y}$ = dimensional transverse coordinate

y = normalized transverse coordinate, $\bar{y}/h_0$
β = velocity ratio, $u_{\max}/u_{\text{ave}}(x)$
ρ = density
ψ = normalized stream function
Ω = normalized vorticity

Subscripts
0 = leading order, parallel chamber quantities
1 = first-order correction
b = burning surface
x, y = axial or transverse component

Superscript
− = dimensional quantity

*Graduate Research Associate, Marquette University, Department of Mechanical and Industrial Engineering. Member AIAA.

†Jack D. Whitfield Professor of High Speed Flows, Department of Mechanical, Aerospace and Biomedical Engineering. Member AIAA.

‡Boling Chair Professor of Excellence in Propulsion, Department of Mechanical, Aerospace and Biomedical Engineering. Associate Fellow AIAA.

I. Introduction

IN the design of solid rocket motors (SRMs), internal flowfield modeling is of paramount importance in evaluating the impact of mean flow on unsteady wave motions, estimating acoustic energy, predicting the onset of hydrodynamic instability, and assessing velocity and pressure coupling with propellant burning.

Naturally, accurate mathematical modeling of the pressure distribution and velocity profiles are important with respect to the efficient design and manufacture of the structural components that comprise the solid rocket motor.

Over-prediction of the pressure load would result in increased motor fabrication cost and weight which, in turn, would result in a negative impact on motor efficiency. If the pressure load is under-predicted, the potential risks can be catastrophic. Four decades ago, Culick developed a mean flow solution for the internal flowfield of a circular-port solid rocket motor using an inviscid, incompressible and rotational flow model.[1] This profile was used in many studies to predict the pressure variation and combustion instabilities.[2-12] Currently, it is used as a baseline in known ballistic codes such as SSP (Standard Stability Prediction).[13-15]

Modern solid rocket motors are manufactured with small tapers that reduce the contact between the casting mandrels and the propellant during mandrel removal. The small, divergent angles aid in the reduction of shear stress on the surface of the propellant. This minimizes the likelihood of propellant tearing, cracking and debonding. Tapers are also used to shape the thrust time curve and to soften thrust transients at tail-off. As a result, tapers are often used in high speed interceptor vehicles requiring thrust curve modifications. Tapers also minimize erosive burning effects and maximize volumetric loading fraction. This helps to increase the port-to-throat area ratio. The problem is that some ballistic codes used to assess the physical characteristics of solid rocket motors do not account for the small tapered angles currently found in modern solid rocket motors. This point was first raised by Clayton[16] in his original investigation of this generally overlooked feature of SRM analysis.

The issue here is that when ballistic codes refer to Culick's[1] or Taylor's[17] profiles to evaluate tapered solid rocket motors, the pressure drop can be over-predicted by as much as 25% to 80%. This is due to the velocity diminution that accompanies cross-sectional area increases. Naturally, with an increase in flow area (decrease in velocity), the dynamic pressure becomes smaller, leading to an overall decrease in total pressure drop. In an effort to produce a solution that yields the proper pressure correction applicable to tapered combustion chambers, Clayton was able to obtain an approximate solution by employing a regular perturbation method.[16] Being asymptotic, Clayton's solution was shown to be reducible, at leading order, to Culick's profile for a taper angle of zero.

In 1956, Taylor[17] derived the solution for a rectangular chamber with porous walls as part of his treatment of pressure-driven flows in wedges and cones. Other pertinent solutions were later advanced by Yuan and Finkelstein[18,19] and Terrill[20] who incorporated the effects of viscosity in both axisymmetric and planar domains. Their work was recently extended to include the effects of wall regression by Majdalani, Vyas and Flandro,[21] and Zhou and Majdalani.[22]

The physical model to be employed here consists of the straight section of the motor and the tapered section as well. The incorporation of the taper in the context of internal flowfield studies of solid rocket motors seems to have received very little attention. In fact, one may find very few studies concerned with tapered chambers. One such study may be attributed to the work of Mu-Kuan and Tong-Miin.[23] In their attempt to understand the flowfield present in tapered ducts applicable to solid propellants, Mu-Kuan and Tong-Miin conducted a fiber optic study of a non-uniform, injection induced flow in tapered channels. The principal focus of their study was to determine the effect of the divergent configuration on the promotion of flow stability. Their study also confirmed the lack of similarity between the velocity distributions in straight (non-tapered) and tapered chambers. It can hence be seen that the problem concerning solid rocket motors with tapered walls will serve more than one purpose; particularly, it will help to elucidate the contrasting mean velocity distributions and compare the pressure drop between the parallel and tapered motor shapes. It will also address the mathematical peculiarities associated with the no-slip condition along the tapered surface.

In searching for a solution that captures the effects of the tapered walls, the methodology utilized in this analysis will exploit the vorticity at the surface and its transport along the streamlines. This vorticity is the result of the axial pressure gradient. The relationship between these key variables permits the proper form of chamber vorticity to be ascertained. The development of an expression for the vorticity particular to tapered geometry results in a nonlinear governing differential equation, for which a solution may be obtained by the method of regular perturbations.

Accompanying the perturbation solution, an alternate solution will be sought using the method of variation of parameters. The solution obtained by this technique will be found to be identical to the leading-order solution provided by the regular perturbation method, thereby legitimizing the approach used to resolve the problem under study. Finally, a numerical simulation will be performed with the aim of validating both forms of the analytical solution. At the conclusion of this study, an error analysis will be used to establish the physical limitations and bracket the applicability range of the proposed analytical expressions.

American Institute of Aeronautics and Astronautics

II.   Mathematical Model

The idealized tapered slab burner is characterized as a rectangular, parallel port duct with the top and bottom porous surfaces oriented at an angle α. The model presented in Fig. 1 incorporates both geometries. This allows one to account for the bulk flow originating from the non-tapered section of the motor. Accordingly, the origin for the coordinate system is expediently placed at the interface where $\bar{x}$ and $\bar{y}$ denote the axial and transverse coordinates, respectively. The non-tapered section of the motor has dimensions of length L_0, height $2h_0$, and width w_0. The gases are injected across the top and bottom surfaces in a normal and uniform manner. As a consequence of mass conservation, the injected gases are forced to turn and assimilate with the primary bulk flow emanating from the straight section of the motor (see Fig. 1a).

A.   Governing Equations

Conceptualizing the problem at hand, it is instructive to note that the vorticity produced at the surface is an outgrowth of the interaction between the injected fluid and the axial pressure gradient. This phenomenon allows one to utilize an alternate form of Euler's momentum equation and its explicit relationship between chamber pressure and vorticity. Another feature of this governing set is that the vorticity is expressed in terms of the stream function. For the planar, two-dimensional model proposed, the flow can be characterized as (i) steady, (ii) inviscid, (iii) incompressible, (iv) rotational, and (v) non-reactive. In accordance with the stated assumptions, the kinematic equations of motion can be written in vector and scalar notations. Hence,

$$\bar{\boldsymbol{u}} \cdot \bar{\nabla} \boldsymbol{u} = -\bar{\nabla} p \tag{1}$$

$$-\bar{\Omega}_z = \bar{\nabla}^2 \bar{\psi} \tag{2}$$

$$\bar{u}_x \frac{\partial \bar{u}_y}{\partial \bar{x}} + \bar{u}_y \frac{\partial \bar{u}_y}{\partial \bar{y}} = -\frac{1}{\bar{\rho}} \frac{\partial \bar{p}}{\partial \bar{y}} \tag{3}$$

$$\bar{u}_x \frac{\partial \bar{u}_x}{\partial \bar{x}} + \bar{u}_y \frac{\partial \bar{u}_x}{\partial \bar{y}} = -\frac{1}{\bar{\rho}} \frac{\partial \bar{p}}{\partial \bar{x}} \tag{4}$$

$$-\bar{\Omega}_z = \frac{\partial^2 \bar{\psi}}{\partial \bar{x}^2} + \frac{\partial^2 \bar{\psi}}{\partial \bar{y}^2} \tag{5}$$

B.   Boundary Conditions

Judicious boundary conditions are needed to obtain a closed-form solution that is representative of the physical model. To begin, one must recognize that the transverse component of velocity cannot physically contribute to the axial flow crossing into the tapered region at $\bar{x} = 0$ (see Fig. 2). The needed boundary conditions are prescribed as follows: (i) inflow across the tapered interface must originate from the outflow of the non-tapered segment of the motor; (ii) no flow across the midsection plane; and (iii) uniform and constant, normal injection at the burning surface. Mathematically, these conditions are expressed as:

$$\begin{cases} \bar{x} = 0, \ \forall \bar{y}, \ \bar{u}_x = \frac{1}{2} \pi V_b \left(L_0 / h_0 \right) \cos\left(\frac{1}{2} \pi \bar{y} / h_0 \right) \\ \bar{y} = \bar{y}_s, \ \forall \bar{x}, \ \bar{u}_x = V_b \sin \alpha \\ \bar{y} = \bar{y}_s, \ \forall \bar{x}, \ \bar{u}_y = -V_b \cos \alpha \\ \bar{y} = 0, \ \forall \bar{x}, \quad \bar{u}_y = 0 \end{cases} \tag{6}$$
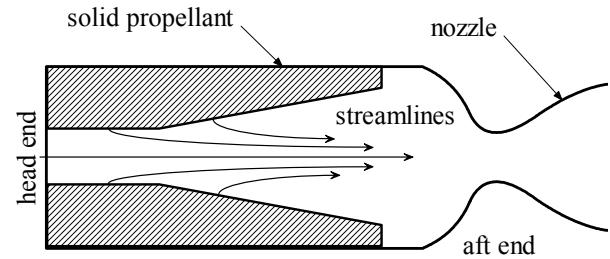
a)
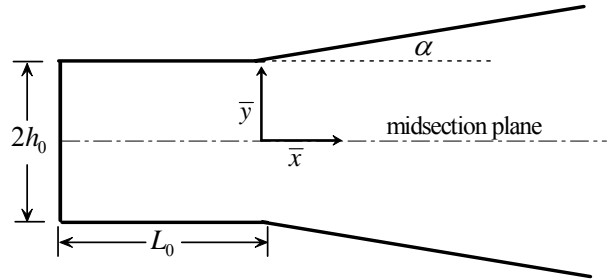
b)

Fig. 1 Schematic featuring a) typical slab burner configuration with tapered walls and b) coordinate system used for the mathematical model.
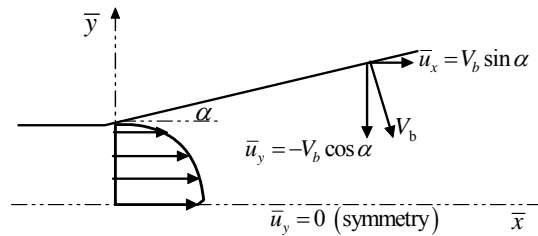
Fig. 2 Graphical depiction of the tapered segment with corresponding boundary conditions.

C. Normalization

Normalization of the governing variables aids in the derivation of a clear solution that describes the flowfield in a succinct manner. Here, we use

$$x = \frac{\overline{x}}{h_0}; \ y = \frac{\overline{y}}{h_0}; L = \frac{\overline{L}_0}{h_0}; \ \nabla = h_0 \overline{\nabla} \tag{7}$$

$$u_x = \frac{\overline{u}_x}{V_b}; \ u_y = \frac{\overline{u}_y}{V_b}; \ p = \frac{\overline{p}}{\rho V_b^2} \tag{8}$$

$$\psi = \frac{\overline{\psi}}{h_0 V_b}; \ \Omega = \frac{h_0 \overline{\Omega}}{V_b} \tag{9}$$

Along with the non-dimensional variables, the normalization of the boundary conditions yields

$$\begin{cases} x = 0, \ \forall y, \quad u_x = \frac{1}{2}\pi L \cos\left(\frac{1}{2}\pi y\right) \\ y = y_s, \ \forall x, \ u_x = \sin\alpha \\ y = y_s, \ \forall x, \ u_y = -\cos\alpha \\ y = 0, \ \forall x, \quad u_y = 0 \end{cases} \tag{10}$$

D. One-Dimensional Velocity

The tapered slab geometry is based on the Cartesian coordinate system (as depicted in Fig. 1b) where $\overline{x}$ is the dimensional axial coordinate and $\overline{y}$ is the dimensional transverse coordinate. The area of the tapered burning surface is given by

$$A_b = w_0 \overline{x} \sec\alpha \tag{11}$$

The chamber cross-sectional area may be evaluated from

$$A(\overline{x}) = w_0 \left(h_0 + \overline{x} \tan\alpha \right) \tag{12}$$

The inflow cross-sectional area at the interface of the tapered and straight portions of the chamber is given by

$$A_0 = w_0 h_0 \tag{13}$$

The corresponding velocity becomes

$$\overline{u}_0 = (L_0 / h_0) V_b \tag{14}$$

Here L_0 can be defined as the bulk flow parameter because it is directly proportional to the average velocity at the entrance to the tapered portion. Due to mass conservation, the cross-sectional average velocity of the fluid at any axial location $\overline{x}$ may be expressed by

$$\overline{u}_{ave}(\overline{x}) = \frac{A_0 \overline{u}_0 + A_b V_b}{A(\overline{x})} \tag{15}$$

By substituting Eqs. (11)–(14) into Eq. (15) and expressing the resulting relation in normalized variables one gets

$$u_{ave}(x) = \frac{L + x \sec\alpha}{1 + x \tan\alpha} \tag{16}$$

For the case of $\alpha = 0$, Eq. (16) reduces to

$$u_{ave} = L + x \tag{17}$$

which depicts the bulk flow in a straight duct with uniform inflow.

To gain an in-depth understanding of the behavior of the bulk flow in tapered chambers at lengths sufficiently removed from the interface, one may manipulate Eq. (16) and compute the limit. Doing so one obtains

$$u_{ave}(x) = \left(Lx^{-1} + \sec\alpha\right)\left(x^{-1} + \tan\alpha\right)^{-1} \tag{18}$$

Evaluating the limit at $x \to \infty$ gives

$$\lim_{x \to \infty} u_{ave}(x) = \csc\alpha \tag{19}$$

As seen in Eq. (19), the average velocity in a tapered chamber converges to a constant value as the axial distance approaches infinity (except for $\alpha = 0$). The result is due to mass conservation. The presence of the taper increases the flow area, attenuating the acceleration of the gases. Consequently, the velocity converges to a constant value, whereas the gases in a parallel chamber continue to accelerate at a constant rate. This behavior is clearly illustrated in Fig. 3. The fact that the bulk flow velocity converges to a constant value suggests that the geometry imposes a restriction on the flow behavior. For a combined motor configuration, the parallel segment is followed by the tapered segment of the motor (see Fig. 1). Knowing that the average velocity in a tapered chamber must converge to a constant value, it is not physically possible for the average velocity in the motor to increase beyond the limit prescribed by the tapered segment of the chamber. To suggest otherwise would constitute a violation of continuity. Hence, the average velocity must be less than or equal to the maximum velocity that can be attained in a tapered motor. Mathematically, this can be expressed by
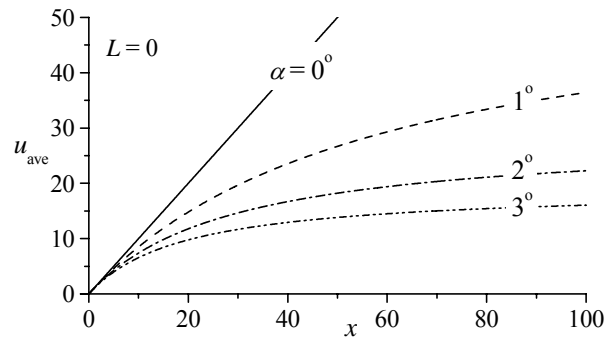
Fig. 3 Plot of average velocity down the channel as a function of taper angle.

$$u_{\text{ave}}(x)\big|_{\alpha=0^\circ} \le u_{\text{ave}}(\infty) \Rightarrow L + x \le \csc\alpha \qquad (20)$$

Rearranging and expressing the result from Eq. (20) in dimensional variables, one obtains

$$\alpha\left(L_0 + \bar{x}\right) \le h_0 \qquad (21)$$

where $\alpha \approx \sin\alpha$ for small values of α. The selection of geometric motor parameters that satisfy Eq. (21) ensures that the solution does not violate continuity.

E. Stream Function along the Burning Surface

A crucial component to the formulation of the flowfield under study is the development of the stream function at the simulated burning surface. The nature of the stream function changes with the angular orientation of the burning surface. Therefore, one can define the directional derivative along the burning surface as

$$\frac{d\psi_s}{ds} = \frac{\partial\psi}{\partial x}\cos\alpha + \frac{\partial\psi}{\partial y}\sin\alpha \qquad (22)$$

Along the burning surface (see Fig. 4), the normalized variables are evaluated to be

$$x = s\cos\alpha \qquad (23)$$

$$y_s = 1 + x\tan\alpha \qquad (24)$$

$$u_x = \sin\alpha \qquad (25)$$

$$u_y = -\cos\alpha \qquad (26)$$

Making use of the stream function relations as defined at the burning surface, one puts

$$u_x = \frac{\partial\psi}{\partial y}, \quad u_y = -\frac{\partial\psi}{\partial x} \qquad (27)$$

Subsequent insertion of the stream function definitions into Eq. (22) yields

$$\frac{d\psi_s}{ds} = \cos^2\alpha + \sin^2\alpha \Rightarrow \frac{d\psi_s}{ds} = 1 \qquad (28)$$

Integrating the resulting expression and converting back to the spatial coordinates, one obtains
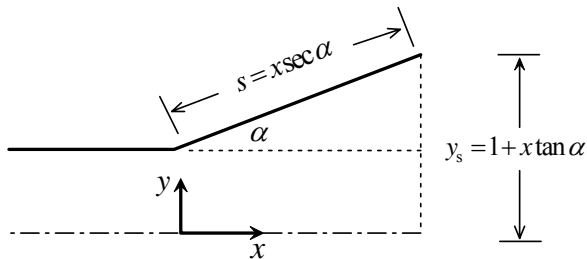
Fig. 4 Schematic of tapered segment showing key geometric parameters in dimensionless form.

$$\psi_s(s) = s \Rightarrow \psi_s(x) = x\sec(\alpha) + C \qquad (29)$$

where C is a constant that can be evaluated by applying the boundary condition, $\psi_s(0) = L$. Application of this constraint gives

$$\psi_s(x) = x\sec\alpha + L \qquad (30)$$

F. Axial Pressure Gradient

Essential to the development of the chamber vorticity is the derivation of the axial pressure gradient. By close inspection it is evident that the axial pressure gradient is the primary source of vorticity and aids in its transport along the streamlines. This alludes to the idea that it is quite advantageous to exploit the relationship between the pressure gradient and the vorticity as a means to arrive at a suitable form for the chamber vorticity. To begin, one may start by expressing Bernoulli's equation along the central streamline as

$$p(x) = p_0 - \tfrac{1}{2}u_{\max}^2(x) \qquad (31)$$

The total pressure in the combustion chamber of solid rocket motors is sensitive to the shape of the axial profiles. In non-tapered chambers, the shape of the axial profile is determined by the ratio of the axial velocity to the axial distance. For diverging ducts, the axial profile changes at the burning surface as the gases move downstream. Thus, it is required that the shape of the profile be known at each axial location in order to obtain accurate pressure estimates. Considering that the maximum velocity is unknown, it is expedient to define a ratio between the maximum and average local velocities at any axial location x. This velocity ratio can be written as

$$\beta(x) = \frac{u_{\max}}{u_{\text{ave}}(x)} \qquad (32)$$

The form of $\beta(x)$ will be later determined to satisfy the no-slip condition along the tapered burning surface. By substituting Eq. (32) into Eq. (31), the expression becomes

$$p(x) = p_0 - \tfrac{1}{2}\beta^2 u_{\text{ave}}^2(x) \qquad (33)$$

The pressure gradient can be determined along the surface by calculating the derivative of Eq. (33). The result is

$$\frac{dp}{dx} = -\beta^2(x)\bar{u}(x)\left[\frac{d\bar{u}(x)}{dx} + \frac{\bar{u}(x)}{\beta(x)}\frac{d\beta(x)}{dx}\right] \qquad (34)$$

Differentiating Eq. (16) and substituting the known surface variables furnishes

$$\frac{du_{\text{ave}}}{dx} = \frac{\sec\alpha}{y_s} - \frac{\psi_s\tan\alpha}{y_s^2} \qquad (35)$$

By substituting Eq. (35) into Eq. (34) and simplifying, it follows that

$$\frac{\mathrm{d}p}{\mathrm{d}x} = -\frac{\beta^2 \psi_s \sec\alpha}{y_s^2}\left[1 - \frac{\psi_s \tan\alpha}{y_s} + \psi_s \cos\alpha\left(\frac{\beta'}{\beta}\right)\right] \quad (36)$$

where

$$\beta' = \frac{\mathrm{d}\beta}{\mathrm{d}x} \quad (37)$$

G. Surface Vorticity

The relationship between the chamber vorticity and pressure is now established. Moving forward, one may seek evaluation of the momentum equation for steady, inviscid flows at the surface. Recalling the normalized form of Euler's momentum equation for steady, incompressible and inviscid flows,

$$\mathbf{u} \cdot \nabla \mathbf{u} = -\nabla p / \rho \quad (38)$$

one may substitute the well known vector identity, $\mathbf{u} \cdot \nabla \mathbf{u} = \nabla \frac{1}{2} \mathbf{u} \cdot \mathbf{u} - \mathbf{u} \times \nabla \times \mathbf{u}$, to obtain an alternate expression of the form

$$\mathbf{u} \times \boldsymbol{\Omega} = \nabla\left(p + \tfrac{1}{2}\mathbf{u} \cdot \mathbf{u}\right) \quad (39)$$

The velocity vector at the simulated burning surface is defined as

$$\mathbf{u} = \sin\alpha\hat{\boldsymbol{i}} - \cos\alpha\hat{\boldsymbol{j}} \quad (40)$$

Evaluating the expression at the surface by substitution of Eq. (40) into (39) gives

$$\mathbf{u} \times \boldsymbol{\Omega} = -\Omega_s\left(\sin\alpha\hat{\boldsymbol{i}} - \cos\alpha\hat{\boldsymbol{j}}\right) = -\Omega_s\hat{\boldsymbol{s}} \quad (41)$$

where $\hat{s}$ represents the unit vector parallel to the burning surface. As we treated the directional derivative of the stream function along the surface, the chain rule can be applied to the pressure gradient parallel to the burning surface. Hence, one can put

$$\frac{\mathrm{d}p}{\mathrm{d}s}\hat{\boldsymbol{s}} = \left[\frac{\mathrm{d}p}{\mathrm{d}x}\cos\alpha + \frac{\mathrm{d}p}{\mathrm{d}y}\sin\alpha\right]\hat{\boldsymbol{s}} \quad (42)$$

Equating the expressions provided by Eqs. (41) and (42) yields

$$\Omega_s = -\frac{\mathrm{d}p}{\mathrm{d}x}\cos\alpha - \frac{\mathrm{d}p}{\mathrm{d}y}\sin\alpha \quad (43)$$

Considering values of α between $1°$ and $3°$, any term containing $\sin\alpha$ would appear to be negligible. Taking this into account, Eq. (43) can be reduced to

$$\Omega_s = -\frac{\mathrm{d}p}{\mathrm{d}x}\cos\alpha + O\left(\alpha V_b^2\right) \quad (44)$$

Having previously formulated an expression for the pressure gradient, the surface vorticity can be expressed as

$$\Omega_s = -\frac{\beta^2 \psi_s}{y_s^2}\left[1 - \frac{\psi_s \sin\alpha}{y_s} + \psi_s \cos\alpha\left(\frac{\beta'}{\beta}\right)\right] \quad (45)$$

Figure 5 allows one to visually interpret the pertinent surface and chamber quantities that are essential to formulate the governing equation for mean flow in tapered ducts. Shown in the diagram are the domains for which the required form of the vorticity is given. Also shown are the values of the stream function at the boundaries, which will be used later to obtain a closed-form solution.

III. First Solution: Regular Perturbations

At this point, one may recall that vorticity is produced at the surface from the interaction between the perpendicularly injected gases and the axial pressure gradient. The primary feature particular to the vortical behavior of an inviscid fluid is the fact that the vorticity generated at the surface is transported along the streamlines as the gases penetrate into the chamber. The idea that the vorticity is conserved in inviscid systems suggests that the expression for the surface vorticity is now valid (along the streamlines) throughout the chamber. Therefore, one may remove the subscript from the stream function and vorticity variables in Eq. (45). Next, one may equate Eq. (3)
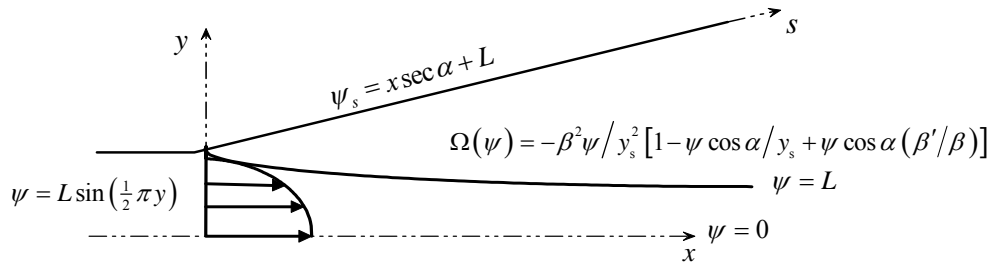
Fig. 5 Evaluation of the stream function along the boundaries. Also shown is the key relation linking vorticity at any point along a streamline to the stream function at the surface; the latter remains constant along any streamline crossing the chamber length.

with Eq. (45) to obtain a partial, nonlinear differential equation that governs the flow. Equating these expressions, one finds

$$\frac{\partial^2 \psi}{\partial x^2} + \frac{\partial^2 \psi}{\partial y^2} = -\frac{\beta^2 \psi}{y_s^2}\left[1 - \frac{\psi \sin \alpha}{y_s} + \psi \cos \alpha \left(\frac{\beta'}{\beta}\right)\right] \quad (46)$$

The boundary conditions required to solve Eq. (46) are given as

$$\psi(x,0) = 0, \quad \psi(x,y_s) = \psi_s \quad (47)$$

For the cylindrical case, Clayton[16] determined the relative magnitudes of the axial derivatives of the stream function and the velocity ratio by numerical analysis. Based on his results, he was able to deduce that the axial derivatives were negligibly small. In particular, Clayton noted that β' and $\partial^2 \psi / \partial x^2$ were small quantities. Clayton's observations may be verified using a scaling analysis. Considering that

$$\frac{\partial^2 \psi}{\partial x^2} = \frac{\partial u_y}{\partial x} \quad (48)$$

one may recall that the transverse velocity is independent of x in the straight channel, thus causing Eq. (48) to vanish. Evidently, the presence of a small taper will not affect the size of this term. Therefore, the axial derivatives are small and can be neglected in the prescribed tapered domain. Once the proper form of the velocity ratio has been obtained, a scaling analysis will be employed once more to further justify neglecting β'. Using arguments similar to those provided by Clayton, one can reduce Eq. (46) into

$$\frac{\partial^2 \psi}{\partial y^2} = -\frac{\beta^2 \psi}{y_s^2}\left(1 - \frac{\psi \sin \alpha}{y_s}\right) \quad (49)$$

Recognizing that the reduced equation is nonlinear, a solution can be sought by the method of regular perturbations. Accordingly, the stream function and velocities are expanded in the form

$$\psi = \psi_0 + \psi_1 \varepsilon + O\left(\varepsilon^2\right) \quad (50)$$

$$u_s = u_{s,0} + u_{s,1} \varepsilon + O\left(\varepsilon^2\right) \quad (51)$$

Similarly, by expanding Eq. (32) in an effort to assure satisfaction of the no-slip condition along the tapered surface, one obtains

$$\beta_s = \beta_0 + \beta_1 \varepsilon + O\left(\varepsilon^2\right) \quad (52)$$

where the perturbation parameter is due to the small taper angle, namely,

$$\varepsilon = \sin(\alpha) \quad (53)$$

The governing equation can be solved by first inserting Eq. (50) and Eq. (52) into Eq. (49) and expanding the resulting terms. This method serves to linearize the governing equation by reducing it to a sequence of linear problems, making a solution by standard methods accessible.

A. Leading-Order Solution

For the sake of brevity, the details of the expansion are not presented here. At leading order, $O(1)$, one obtains

$$\frac{d^2 \psi_0}{dy^2} + \frac{\beta_0^2 \psi_0}{y_s^2} = 0 \quad (54)$$

This is a second-order, linear differential equation that allows for the simple extraction of the transverse variation of the stream function. The general solution can be expressed as

$$\psi_0(y) = C_1 \cos\left(\beta_0 \frac{y}{y_s}\right) + C_2 \sin\left(\beta_0 \frac{y}{y_s}\right) \quad (55)$$

Now that a general solution has been obtained, evaluation of Eq. (55) at the conditions provided by Eq. (47) furnishes the leading-order solution,

$$\psi_0(y) = \psi_s \sin\left(\beta_0 \frac{y}{y_s}\right) \quad (56)$$

where

$$\psi_s = x \sec \alpha + L \text{ and } \beta_0 = \tfrac{1}{2}\pi \quad (57)$$

It should be noted that at $L = \alpha = 0$, one recovers

$$\psi_0(y) = x \sin(\beta_0 y) \quad (58)$$

Equation (58) represents Taylor's profile for porous flow in channels.[17] The leading-order solution, given by Eq. (56), can be described as an expanded version of the Taylor profile. Such a form can be attributed to the additional bulk flow resulting from increased surface area owing to the divergent angle of the burning surface.

B. First-Order Solution

At first order, the perturbative expansion yields

$$\frac{d^2 \psi_1}{dy^2} + \frac{\beta_0^2 \psi_1}{y_s^2} + \frac{2\beta_0 \beta_1 \psi_0}{y_s^2} - \frac{\beta_0^2 \psi_0^2}{y_s^3} = 0 \quad (59)$$

The first-order boundary conditions are

$$\psi_1(0) = 0, \quad \psi_1(y_s) = 0 \quad (60)$$

By application of these boundary conditions, one obtains a first-order correction of the form

$$\psi_1(x,y) = \frac{\psi_s^2}{6y_s}\left[3 - 4\cos\left(\frac{\beta_0 y}{y_s}\right) + \cdots\right.$$

$$\left. + \cos\left(\frac{2\beta_0 y}{y_s}\right) - 2\sin\left(\frac{\beta_0 y}{y_s}\right) + 6y\beta_1 \cos\left(\frac{\beta_0 y}{y_s}\right)\right] \quad (61)$$

The first-order correction accounts for transverse expansion, flow deceleration and the axial derivatives. Observing Eq. (61), it can be seen that there exists an unknown term that orginates from the perturbed velocity ratio β. The final step in the solution process involves solving for the first-order velocity ratio β_1, such that the no-slip condition is satisfied along the tapered surface. In the process, it is neccesary to express the surface velocity using

$$u_s = u_{y,s}\cos(\alpha) - u_{x,s}\sin(\alpha) = u_{s,0} + u_{s,1}\varepsilon \quad (62)$$

and so

$$u_s = \frac{\partial \psi}{\partial y}\cos(\alpha) + \frac{\partial \psi}{\partial x}\sin(\alpha) =$$

$$(\psi_0 + \psi_1\varepsilon)_y \cos(\alpha) + (\psi_0 + \psi_1\varepsilon)_x \sin(\alpha) \quad (63)$$

Considering that ψ_0 already satsifies the no-slip condition at the wall, one may segregate the first-order correction by putting

$$u_{s,1} = \frac{\partial \psi_1}{\partial y}\cos(\alpha) + \frac{\partial \psi_1}{\partial x}\sin(\alpha) \quad (64)$$

Again, it can be seen that the term containing $\sin(\alpha)$ is negligibly small, being of $O(\varepsilon)$. One may neglect this term and set Eq. (64) equal to zero. Evaluating the resulting expression at the tapered surface, one obtains

$$\beta_1 = 2/(3y_s) \quad (65)$$

The required form of the leading and first-order velocity ratios, β_0 and β_1, is now determined. At this point, it is necessary to make use of a scaling analysis to justify neglecting their derivatives. Expressing Eq. (65) in the form of its derivative, one can put

$$\beta_s' = \beta_0' + \psi_s'\beta_1'\varepsilon + O(\varepsilon^2) \quad (66)$$

Using the known values of the velocity ratios, it follows that

$$\beta_s' = \tfrac{2}{3}\sin\alpha \left(\psi_s/y_s\right)' \quad (67)$$

Computing the derivative, one obtains

$$\beta_s' = -\tfrac{2}{3}(1 + x\tan\alpha)^{-2}\frac{\sin^2\alpha}{\cos^2\alpha} \approx O(\varepsilon^2) \quad (68)$$

IV.   Method of Variation of Parameters

Using the method of variation of parameters, a more general solution that depicts the behavior of the governing equation may be sought. For purposes of obtaining an approximate solution, the distance from the midsection plane to the simulated burning surface is again approximated as a constant although it is a function of x. One may begin unraveling the solution

by recalling the governing equation, as derived in the previous section, from Eq. (46), as

$$\frac{\partial^2\psi}{\partial x^2} + \frac{\partial^2\psi}{\partial y^2} = -\frac{\beta^2\psi}{y_s^2}\left[1 - \frac{\psi\sin\alpha}{y_s} + \psi\cos\alpha\left(\frac{\beta'}{\beta}\right)\right] \quad (69)$$

Commensurate with the approximations considered for the perturbation solution, the governing equation reduces to

$$\frac{\partial^2\psi}{\partial x^2} + \frac{\partial^2\psi}{\partial y^2} + \frac{\beta^2\psi}{y_s^2} = 0 \quad (70)$$

Treating y_s as a constant, the most general solution assumes the form

$$\psi(x,y) = C_1(x)\sin\left(\beta\frac{y}{y_s}\right) + C_2(x)\cos\left(\beta\frac{y}{y_s}\right) \quad (71)$$

Inserting Eq. (71) into Eq. (70), one finds that

$$\psi(x,y) = (K_1 x + K_2)\sin\left(\beta\frac{y}{y_s}\right) + (K_3 x + K_4)\cos\left(\beta\frac{y}{y_s}\right)$$

$$(72)$$

The surface boundary conditions can be determined by evaluating the stream function at the surface. Referring back to the previous section, it may be recalled that

$$\psi_s = x\sec\alpha + L \quad (73)$$

In order to obtain the proper boundary conditions at the surface, one may employ the definition of the stream function. Doing so yields

$$u_x = \left.\frac{\partial \psi_s(x,y_s)}{\partial y}\right|_{\forall x} = 0 \quad (74)$$

and

$$u_y = \left.-\frac{\partial \psi_s(x,y_s)}{\partial x}\right|_{\forall x} = -\sec\alpha \quad (75)$$

Due to the quasi-developed flow entering from the non-tapered segment of the motor, one may observe that there exists an inflow boundary condition at the interface. This condition has been previously referred to as the bulk flow parameter and is expressed mathematically by

$$u_x = \left.\frac{\partial \psi_s(0,y_s)}{\partial y}\right|_{\forall y} = -L\frac{\pi}{2y_s}\cos\left(\frac{\pi y}{2y_s}\right) \quad (76)$$

The final boundary condition requires no flow across the midsection plane. It is also referred to as the condition for symmetry. This is expressed as

$$u_y = \left.-\frac{\partial \psi_s(x,0)}{\partial x}\right|_{\forall x} = 0 \quad (77)$$

A. Particular Solution

In searching for a particular solution, one may now apply the aforementioned boundary conditions. Application of the condition for symmetry reduces the general expression to

$$\psi(x, y) = (K_1 x + K_2) \sin\left(\beta \frac{y}{y_s}\right) \qquad (78)$$

Next, the no-slip condition at the simulated burning surface yields

$$u_x = \left. \frac{\partial \psi_s(x, y_s)}{\partial y} \right|_{\forall x} = 0 \, ,$$

$$\Rightarrow \cos(\beta) = 0 \Rightarrow \beta = (2n+1)\frac{\pi}{2}, \; n = 0 \qquad (79)$$

For uniform, normal injection at the simulated burning surface, the boundary condition can be expressed as

$$u_y = \left. -\frac{\partial \psi_s(x, y_s)}{\partial x} \right|_{\forall x} = -\sec \alpha$$

$$\Rightarrow C_1 \sin\left(\frac{\pi}{2}\right) = -\sec \alpha \Rightarrow C_1 = -\sec \alpha \qquad (80)$$

The final constant of integration is determined by matching the bulk flow condition at the interface of the taper. Doing so, one acquires

$$C_2 \frac{\pi}{2 y_s} \cos\left(\frac{\pi y}{2 y_s}\right) = -L \frac{\pi}{2} \cos\left(\frac{\pi}{2} y\right) \Rightarrow C_2 = -L \qquad (81)$$

Finally, the particular solution becomes

$$\psi(x, y) = -(x \sec \alpha + L) \sin\left(\beta \frac{y}{y_s}\right) \qquad (82)$$

As seen above, the method of variation of parameters furnishes a solution identical to the leading-order expression provided by the perturbation method. Such an agreement between the two substantiates the legitimacy of the approach used heretofore.

V. Velocity, Pressure and Vorticity

Now that the proper form of the stream function has been ascertained, it is possible to extract other useful physical quantities particular to tapered flowfields. A useful analysis of the remaining flow attributes can be made from both the leading-order and first-order solutions. The incorporation of the first-order correction ensures that the physical characteristics consistent with flow in tapered geometries are recovered at larger taper angles and axial distances. In particular, the addition of higher-order corrections may be deemed necessary for the axial velocity and the pressure drop, ensuring a reasonably accurate solution suitable for comparison with its numerical counterpart.

Although the distance to the tapered surface is a function of the axial coordinate x, it may be treated as a constant in the evaluation of the velocity, pressure, and vorticity. This enables one to express the desired quantities in a compact and concise form similar to the leading-order solution. Forthwith, one can compute the velocity components from the definition of the stream function. At the outset, the leading-order axial velocity component may be written as

$$u_{x,0} = \frac{\beta_0 \psi_s}{y_s} \cos\left(\beta_0 \frac{y}{y_s}\right) \qquad (83)$$

where $\psi_s = x \sec \alpha + L$. The first-order correction for the axial velocity component follows

$$u_{x,1} = \frac{\psi_s^2}{6 y_s^2}\left[-2\beta_0 \cos\left(\beta_0 \frac{y}{y_s}\right) - 2\beta_0 \sin\left(2\beta_0 \frac{y}{y_s}\right) + \cdots \right.$$

$$\left. +6\beta_1 \cos\left(\beta_0 \frac{y}{y_s}\right) - 2\beta_0 (3 y \beta_1 - 2)\sin\left(\beta_0 \frac{y}{y_s}\right)\right] \qquad (84)$$

where the total solution can be concisely expressed as

$$u_x = u_{x,0} + \varepsilon u_{x,1} \qquad (85)$$

At the outset, the leading-order solution for the transverse velocity component is found to be

$$u_{y,0} = -\sec(\alpha)\sin\left(\beta_0 \frac{y}{y_s}\right) + O(\varepsilon) \qquad (86)$$

So far, it has been established that the parameter of interest is the pressure drop. The latter is extremely sensitive to the axial velocity profile which is governed by the height of the chamber. Quite naturally, approximating the chamber height as constant in the axial direction introduces error. That error can be effectively recovered by the addition of the first-order correction.

Having formulated the velocity field, the pressure gradients can be deduced. In order to obtain the required pressure drop along the chamber length, one only needs to insert the axial and transverse velocity relations into the inviscid momentum equations given by Eqs. (4) and (5). By performing this substitution, one gets

$$-\frac{\partial p}{\partial x} = \frac{\pi^2 \psi_s \sec \alpha}{4 y_s^2} \qquad (87)$$

$$-\frac{\partial p}{\partial y} = \frac{\beta_0 \sec^2(\alpha)}{2 y_s^2} \sin\left(\frac{2\beta_0 y}{y_s}\right) \qquad (88)$$

By integrating and combining Eqs. (87) and (88), one is able to produce the spatial variation of the pressure that satisfies both momentum equations. Consequently, the total pressure can be expressed as

$$-p_0(x,y) = \frac{\pi^2}{4y_s^2}\left(\frac{x^2}{2}\sec\alpha + Lx\right) + \cdots$$

$$+\frac{1}{2}\sec^2\alpha\cos^2\left(\beta_0\frac{y}{y_s}\right) + \text{constant} \tag{89}$$

The head-end boundary condition is $p(0,0) = p_{\text{Taylor}}$, where $p_{\text{Taylor}} = -L^2\pi^2/8$. By applying this condition, the constant becomes equal to p_{Taylor}. Setting $\Delta p_0 = p_0(x,y) - p_{\text{Taylor}}$, one can express the leading-order pressure drop in the chamber in the following compact form

$$\Delta p_0 = -\frac{\pi^2}{4y_s^2}\left(\frac{x^2}{2}\sec\alpha + Lx\right) \tag{90}$$

The treatment of y_s as a constant has permitted the development of an approximate expression for the pressure drop at leading order. At this juncture, it may be reasonable to question the accuracy of the expression derived due to the approximations. To arrive at an expression for the pressure drop, y_s has been assumed to be constant twice for purposes of differentiation and once for integration, thereby compounding the errors involved. For larger taper angles, the variation of half-height with axial distance increases, leading to the possibility of the under-prediction of the pressure drop for larger values of α at leading order. In an effort to recover the accuracy of the model presented here, the pressure drop at first-order is considered. The expression is obtained in the same manner as its leading-order solution for pressure with the addition of a term that is of first order. Thus, in the interest of conciseness, the details regarding the derivation are not presented here. The complete relation, including both the leading and first-order terms, at $L = 0$, can be expressed as

$$\Delta p(x;\varepsilon) = -\frac{\pi^2\sec^2\alpha}{12y_s^3}\left(\frac{3}{2}x^2 y_s + \frac{2}{3}x^3\varepsilon\sec\alpha\right) \tag{91}$$

It has been determined earlier that the pressure gradient in the transverse direction is negligibly small. This leaves the axial pressure gradient as the quantity of interest.

In addition to the formulation of the velocity and pressure gradients, one may compute the vorticity in order to complete the extraction of most physical parameters needed to characterize the flowfield. In this effort, the vorticity field can be obtained using

$$\Omega(x,y) = \frac{\partial u_y}{\partial x} - \frac{\partial u_x}{\partial y} \tag{92}$$

Inserting the solutions for the velocity components into Eq. (92) produces the expression for the spatial variation of chamber vorticity. One deduces that

$$\Omega(x,y) = \frac{\beta_0^2\psi_s}{y_s}\sin\left(\beta_0\frac{y}{y_s}\right) \tag{93}$$

Each of the required flowfield characteristics particular to tapered slab burners is now at hand. Although some mathematical similarities *appear* to exist between flow in tapered and straight chambers, models for straight chambers do not encompass all of the physical characteristics inherent in the present model. Since the taper angle is known to be small, it should follow that the leading-order mean flow characteristics possess minimal variance with the taper angle α. However, this is not the case given that the parameter that is most sensitive to the taper appears to be the pressure field.

In order to explore the effects of straight portion of the motor preceding the tapered segment, one may invoke another parameter that arises from this study. This parameter has been described as the bulk flow parameter $L = u_0$; it is also known as the normalized chamber length $L = L_0/h_0$. The bulk flow parameter enables one to examine the physical characteristics of small to moderate size motors with combined geometry.

A. Ideal Momentum Thrust

Considering our efforts to characterize the flowfields in tapered solid rocket motors from a fluid dynamical perspective, further analysis of typical rocket performance parameters require examining the thrust variation with the taper angle α. Effectively, the characterization of the thrust behavior furnishes a link between the mathematical model and standard design procedures. Since the pressure drop is directly related to the thrust, it should follow that both parameters exhibit similar responses to the taper angle. This fact may also confirm the effect that the taper has on the pressure drop in the combustion chambers of current SRMs. To begin, it is helpful to recall the standard form of the momentum equation for a control volume

$$F = \frac{\partial}{\partial t}\int_{cv}\rho V\, d\upsilon + \int_{cs}\rho V(V\cdot\hat{n})\, dA \tag{94}$$

Taking this into account, one may utilize the expression for the average velocity and the chamber cross-sectional area previously derived to aid in the formulation of an expression for the thrust. By recalling these expressions one may put

$$u_{\text{ave}} = \frac{L + x\sec\alpha}{1 + x\tan\alpha} \tag{95}$$

and

$$A(x) = w_0 (1 + x \tan \alpha) \qquad (96)$$

The transient component is not of interest here. Equation (94) becomes

$$F = \int_{cs} \rho V (V \cdot \hat{n}) \, \mathrm{d}A \qquad (97)$$

The definitions of cross-sectional area and average velocity presented in Eq. (95) can be inserted into the steady momentum thrust equation to give

$$F = \rho w_0 (L + x \sec \alpha)^2 \int_{x=0}^{x=L^*} \frac{\mathrm{d}(1 + x \tan \alpha)}{(1 + x \tan \alpha)^2} \qquad (98)$$

Recalling the burning surface definitions of the stream function and chamber height, Eq. (98) can also be expressed as

$$F = \rho w_0 \psi_s^2 \int_{x=0}^{x=L^*} \frac{\mathrm{d}y_s}{y_s^2} \qquad (99)$$

In order to secure an expression that relates the thrust to the taper angle, Eq. (99) must be integrated along the maximum length L^* of the tapered domain. Carrying out the integration, one obtains

$$F = \frac{L^* \rho w_0 \psi_s^2}{L^* + \cot \alpha} \qquad (100)$$

where $\psi_s = L + x \sec \alpha$. To the author's knowledge, this result represents the first analytical expression relating the thrust to tapered geometry, albeit for a non-reactive, incompressible gas.

VI. Added Confirmation: CFD Simulation

Thus far, we have explored the characteristics of mean flowfields applicable to both the slab and cylindrical rocket motors with available analytical procedures. En route to obtaining an analytical solution that encompasses the physical significance of mean flow in tapered and parallel SRM combustion chambers, the first and second-order axial derivatives of the parameters essential to this work were assumed to be negligible. For the case of the tapered cylindrical motor originally formulated by Clayton, a numerical computation was performed in an effort to determine the relative magnitudes of these terms in the governing equations. Close examination of the terms revealed that they were indeed negligible and significant error would not accrue in their absence; hence, an analytical solution was possible by both the method of regular perturbations and variation of parameters. The same reasoning was adopted for the mean flow model in a slab burner. In the same vein, a numerical simulation can now be employed to further assist in the verification and assessment of pertinent parameters critical to the applicability of these closed-form solutions.

At present, a numerical solution would prove to be not only essential, but fundamental to this work in regards to the regular perturbation methods and other approximations used to obtain an explicit analytical solution. A favorable comparison with numerics would serve to further validate the approximate methods used thus far. To that end, a numerical simulation will be pursued. FLUENT, a widely used CFD package in both industry and academia, will be employed to simulate the mean flowfield characteristics of tapered chambers.

A. Geometry and Meshing Scheme

The geometric model for the rectangular geometry is created for taper angles ranging from $1°$ to $3°$. The dimensions are chosen in accordance with the parameters used by the analytical model. The slab is modeled in two-dimensional space with the top and bottom simulated burning surfaces defined as velocity inlets.

The meshing scheme and interval sizes are generally chosen based on the size and complexity of the physical model. Since the model under study possesses relatively simple geometry, standard meshing schemes are utilized to obtain a numerical solution with an interval size of 0.1.

B. Boundary and Operating Conditions

The working fluid is injected at velocities ranging from 0.1 m/s to 1 m/s. These values of injection velocity are chosen in concurrence with the incompressible fluid model which is generally valid for compressible fluids with Mach numbers that are less than 0.3. The selection of the injection velocity can be further validated from experimental work by Brown and co-workers[24-26] as well as a research team led by Dunlap.[27-29] In addition, the selected injection velocity is corroborated by Clayton's CFD results, in which he managed to determine that the taper profiles change minimally with increasing injection velocity (provided that the Reynolds numbers $\mathrm{Re} = \rho V_b D / \mu$ remain within the range of 10^2 to 10^4).[16] The reference pressure can be interpreted as a boundary condition for the stagnation pressure at the head end of the chamber and, as a result, is placed at the origin. This condition is chosen so that the mass outflow condition at the outlet of the chamber is not affected. It also allows the pressure to vanish at the head end.

The theoretical fluid model chosen here for the numerical solution is the laminar model. The flowfield inside an actual solid rocket motor can be turbulent and a significant portion of the combustion occurs near the burning surface so that the chamber is filled primarily with the reaction products (see Chu, Yang and Majdalani[30] and Vyas, Majdalani and Yang[31]).

VII.   Results and Discussion

This section seeks to document and compare the dissimilarities that exist between the numerical and analytical cases presented heretofore. With graphical depictions of the quantities in question, one is able to determine the level of accuracy that is required and which physical parameters are most important. For the case of tapered solid rocket motors, it has been determined that the axial velocity profiles and the pressure drop are of paramount importance. In pursuit of a general expression that describes the flowfield in tapered geometry, some terms were neglected based on generalizations made about the mean flow before a particular solution could be obtained. To validate these, the same problem was solved numerically.

Here, a basic comparison of the solutions obtained by the two methods will be performed with the aim of elucidating the similarities, differences and limitations of the analytical solution. Also in question will be the magnitude of the axial derivatives. This portion of the final analysis will be critical given the assumption of constant distance from the midsection plane to the simulated burning surface.

A.   Pressure Approximations

As seen in Fig. 6a, it is clear that the pressure varies with the taper angle. The slow increase in cross-sectional area acts to decrease the pressure drop by allowing a slight build up in local static pressure resulting from the accompanying decrease in velocity. As it can be inferred from Fig. 6a, larger motors are seen to exhibit a higher sensitivity to small increases in wall taper. Even in chambers with zero bulk flow, one can infer that the influence of minute variations in wall taper can have significant impact on the overall pressure drop. By comparison to Taylor's solution in a straight porous channel, Fig.6a illustrates the dramatic decreases in the absolute pressure drop at higher taper angles taken along the midsection plane $(y = 0)$. In a tapered motor for which the actual pressure drop down the bore is 100 psi, modeling without account for the small taper correction will over-predict the pressure drop to 130-175 psi, for taper angles between $1°$ and $3°$. Naturally, the approximate leading-order solution suggests that these differences become more significant in larger motors for which the constant velocity criterion is not violated. However, using only the leading-order solution to approximate the percent over-prediction can result in exaggerated error estimations. With the addition of the first-order correction, it is observed in Fig. 6b that the percent over-prediction decreases by approximately 10% to 12%, yielding a maximum percent over-prediction of about 63%. The error in predicting the pressure drop without accounting

for wall taper propagates along the midsection plane. As the gases approach the aft end of the motor, the pressure drop can be over-predicted by as much as 38% to 63% for taper angles between $1°$ and $3°$.

The information disclosed in Fig. 6 illustrates the dissimilarities in the pressure drops in tapered and parallel chambers. There are obvious implications associated with ignoring the effect of the taper in ballistic analyses. To that end, one can conclude with certainty that the incorporation of taper in ballistic analyses is necessary to prevent over-prediction of pressure drop, an essential requirement for the manufacture of fail-safe motor casings where precise pressure estimates are highly desirable.
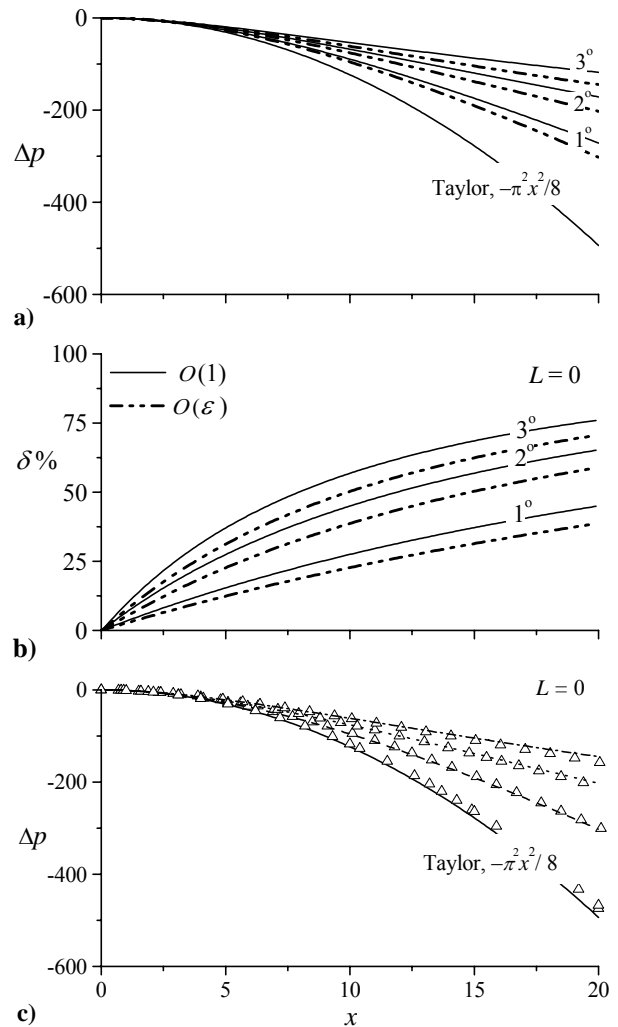
Fig. 6 We plot in a) both leading and first-order pressure drop approximations for several values of taper angle α. In b) the percent over-prediction from a) is calculated and shown at several values of α. In c) we compare numerical versus first-order solutions.

Observing the numerical pressure approximation (shown in Fig. 6c), it is clear that at larger taper angles and longer tapered domains, the numerical and analytical solutions begin to deviate. Any deviation between the analytical and numerical cases can be partly attributed to neglecting the transverse pressure effects in the analytical solutions. Since the half-height and radius increase with axial distance, the transverse terms seem to become somewhat more significant farther away from the head end of the motor. As a result, there is a larger overall transverse contribution to the spatial variation of the pressure over the length of the chamber. Although the higher-order analytical expression accounts for the axial derivatives as well as the transverse expansion, the effects of the constant wall distance assumption begin to manifest in long tapered domains. This can also cause deviations to build up between the numerical and analytical solutions.

The analytical solution seems to consistently reproduce the results provided by the numerical model. Furthermore, one may recall that the level of precision is governed by the relationship between the asymptotic limit and the average velocity of the gases (also known as the constant velocity criterion). For tapered domains that do not satisfy the relationship prescribed by the asymptotic limit, one may begin to discern increased deviation between the numerical and analytical solutions.

B. Momentum Thrust Behavior

In Fig. 7, the idealized thrust behavior is quantified and plotted for each value of α along the midsection plane using $\rho w_0 = 1$ and $L = 0$. It should be borne in mind that the expression presented for the thrust is steady-state and cold flow. Also, it does not explicitly account for regressive, progressive or neutral burning profiles typical of actual solid propellant motors. However, since the surface area increases nonlinearly in the axial direction and time, it may be theorized that tapered SRMs are likely to exhibit behavior close to that of a regressive burning motor.

Consider the limiting case for example: if the taper is very large, the presence of the propellant will be compromised to the extent that the thrust will be much smaller than in the case of a non-tapered propellant. Furthermore, with an increase in burning surface area, comes an increase in chamber motor pressure and, hence, in the regression rate that inherently affects the thrust.

In the previous section, it was surmised that the momentum thrust would respond to the taper angle in the same manner as the pressure drop. Observing Fig. 7, it is evident that this would be the case. One may
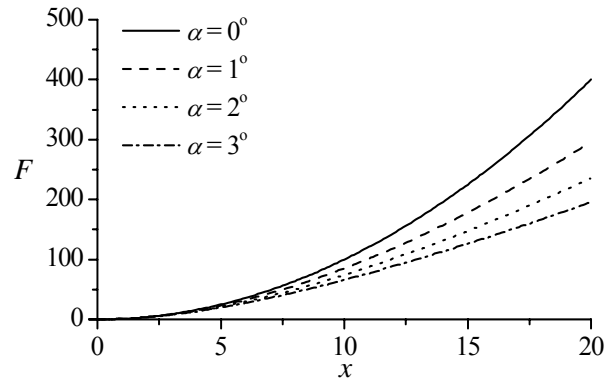
Fig. 7 Idealized momentum thrust along midsection plane at several taper angles. Note that the thrust is overpredicted by internal ballistics not accounting for the presence of taper.

consider that an increase in cross-sectional flow area requires that the average velocity begins to decrease in order to satisfy continuity. As a result, the straight chamber undergoes a faster ascent to its maximum value at the edge of the domain. It is quite possible that current one-dimensional ballistic codes that determine the thrust (with no due attention to the taper), over-predict the average thrust at each axial location.

C. Axial Velocity

Earlier y_s was treated as a constant during the evaluation of the axial and transverse velocity components. By doing so, it was expected that error would be introduced in the solution. Neglecting the axial variation in chamber half-height, it is clear from Fig. 8 that the axial profiles given by the analytical solution for the slab burner tend to slightly undershoot the numerical solution with increasing axial distance. In fact, the discrepancy becomes more appreciable further down the motor chamber and may become non-negligible in very long slab motors.

At this juncture, one should note also that the analytical solutions shown in Fig. 8 include higher-order corrections. Neglecting these higher-order terms leads to a grossly under-predicted maximum velocity. Again, this suggests that the leading-order solution lacks valuable flow information and that the higher-order terms appear to be a requisite for accurate solutions in long chambers with large taper angles (i.e. motors with $L \geq 4$ and $\alpha \geq 2$). The higher order corrections seem to slowly recover the error introduced by neglecting the axial variation of the half-height away from the interface. Nonetheless, Fig. 8 displays very good agreement between the analytical and numerical solutions.

D. Axial Derivatives

Integral to the development of the flowfields discussed throughout this work were the assumptions that led to the dismissal of the axial derivatives. Upon exacting an approximate solution, a scaling analysis was employed during the analytical derivation to determine if, in fact, these assumptions were justifiable. These assumptions targeted two derivatives, namely: (1) $\partial^2\psi/\partial x^2$ and (2) $d\beta/dx$.

The magnitudes of the second-order axial derivatives of stream function have been extracted from the numerical solution and quantified along the midsection plane. The second-order transverse derivatives were also obtained to serve as a basis for comparison. From Fig. 9a, it may be observed that the magnitudes appear to oscillate (as a result of symmetry). More importantly, they remain approximately of $O(10^{-4})$ down the length of each chamber. In contrast, the transverse derivatives $\left(\partial^2\psi/\partial y^2\right)$ shown in Fig. 9b exhibit magnitudes of $O(1)$.

Considering that the axial derivatives are several orders of magnitude smaller than their transverse counterparts, it may be stated that our numerical results confirm the prior scaling analysis that justified their dismissal from the analytical formulation.

In the same vein, it is seen in Fig. 9c that the magnitudes of the axial derivatives for the velocity ratio are small enough that they would have no appreciable effect on the analytical solution. Here too, the numerical results corroborate our original premise behind their dismissal from the analytical solution. The plot shows the axial variation of $d\beta/dx$ at several transverse locations for $\alpha = 3^\circ$. From the figure, it can be deduced that the axial variation of each derivative
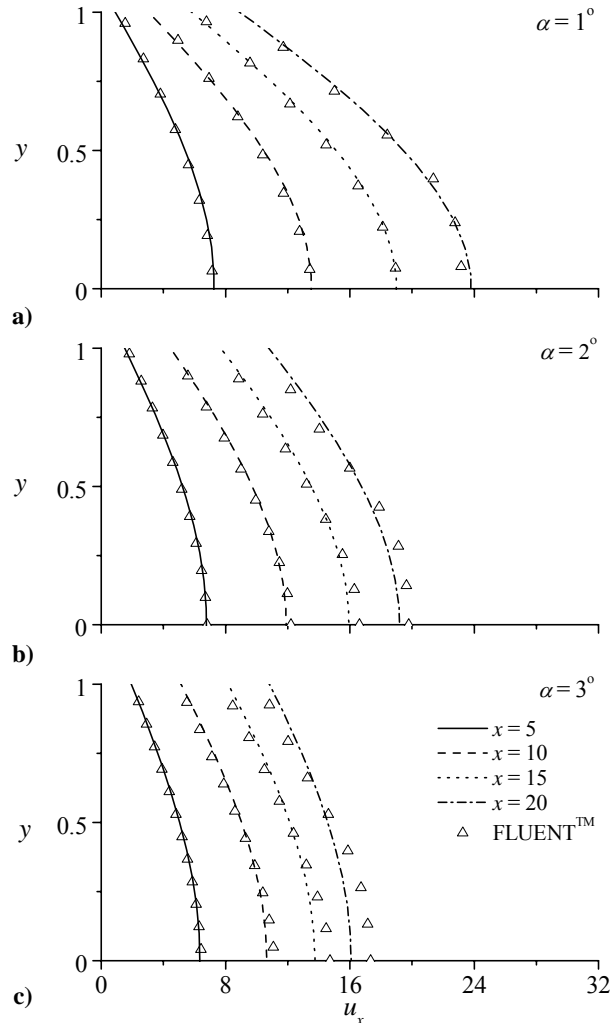
Fig. 8 Numerical versus analytical comparison of slab burner velocity profiles at various locations.
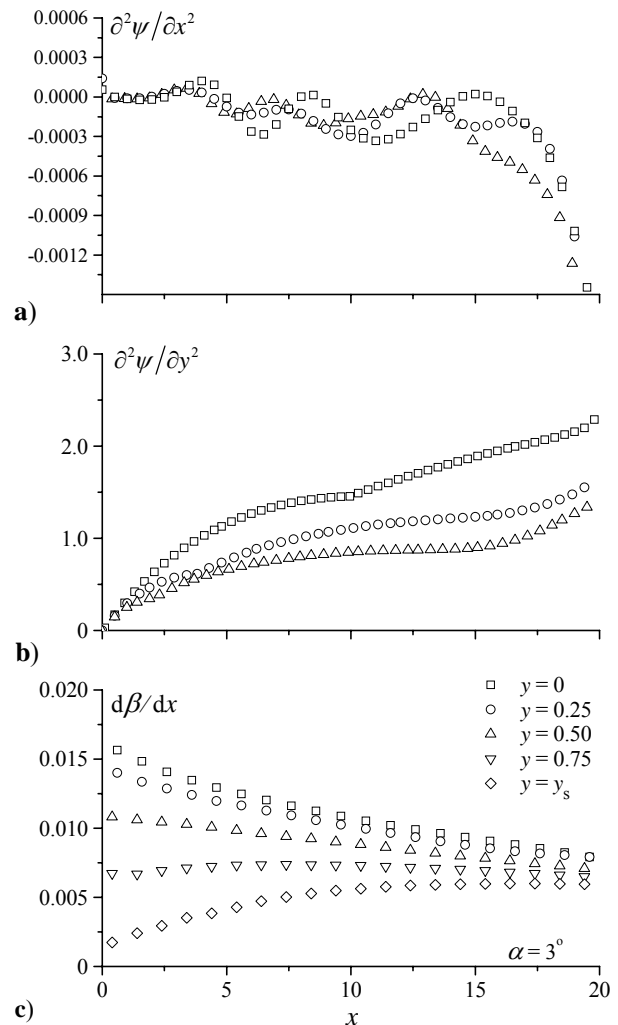
Fig. 9   Derivatives from FLUENT^{TM} shown at several taper angles.

American Institute of Aeronautics and Astronautics

dictates the shape of the velocity profile. For example, at $y = y_s$, the axial derivative slowly increases. One may recall that the velocity profile must adjust itself at each axial location to satisfy the no-slip requirement at the tapered surface. Bearing this in mind, it can be inferred that the rate of change at the wall must increase due to the increased axial variation as the gases propagate down the chamber. Along the midsection, one may notice that the derivative is decreasing. Essentially, this can be ascribed to the maximum velocity decreasing in the axial direction. From a physical standpoint, this must occur in order to satisfy mass conservation. The increasing rate of change at the wall works in conjunction with the decreasing rate of change along the midsection plane to force the profile to slowly relinquish its transverse component with increasing axial distance. Hence, the profile may evolve into a near constant shape over the cross-section perpendicular to the flow for sufficiently long tapered domains. As for the intermediate transverse values, the derivatives exhibit little axial variation being that they are quantified at or near the core of the flow.

VIII. Error Analysis and Limitations

For practical applications of the analytical solutions at increasing orders, one may be concerned with their parametric limitations. Previously, such limitations were explored by analytically predicting the behavior of the gases at an infinite distance away from the head end. The results of this inquiry suggest that some relationships, guided by mass conservation, must be maintained between the geometric parameters. The relationship can be expressed as:

$$\alpha \left(L_0 + \overline{x} \right)/h_0 \leq 1 \qquad (101)$$

This expression was obtained using the average value of the velocity as opposed to the maximum velocity (see Eqs. (20)–(21) for more detail). In order to determine a maximum range for which the analytical solution remains applicable, one must calculate the maximum relative error between asymptotic predictions and numerical solutions. To do so, it is expedient to examine the asymptotic limit where the velocities in each chamber are at their maximum values, specifically, by comparing the maximum velocities predicted by numerics versus asymptotics. For the non-tapered segments, the relationship between maximum and average velocities can be easily found to be

$$u_{\max} = \tfrac{1}{2} \pi u_{\text{ave}} \qquad (102)$$

By translating this result to the maximum velocity, the criteria that establish the upper limit of the solution domain may be extrapolated. One finds

$$\frac{\alpha \left(L_0 + \overline{x} \right)}{h_0} \leq \frac{2}{\pi} \qquad (103)$$

Equation (103), can now be solved for $L_0 = 0$ to obtain the maximum *conservative* domain aspect ratio for a given taper angle. One gets

$$x_{\text{cons}} = \frac{2}{\alpha\pi} \qquad (104)$$

where $x_{\text{cons}} = \overline{x}/h_0$. It is our observation that, so long as $x \leq x_{\text{cons}}$, the percent error between numerics and asymptotics remains less than 1%. The conservative range represents a domain of asymptotic validity in which the accrued error is virtually insignificant. By requiring a minimum chamber aspect ratio of 4 (lest edge effects become important), the maximum conservative taper angle for which an asymptotic solution would exhibit a smaller than 1% error can be calculated from Eq. (104). One finds the maximum conservative taper angle to be 9 degrees. Thus, for the slab burner, a suitable range of tapers would be $0 < \alpha \leq 9^{\circ}$.

In Fig. 10, the numerical and analytical maximum velocities are plotted at several taper angles. Overall, the figures indicate that within the maximum, conservative domain specified by Eq. (104), there is virtually no noticeable deviation between the numerical and analytical solutions (the error remains less than 1%). The issue is, however, the behavior of the fluid once it exits the domain. At this juncture, one must be concerned with the maximum deviation between the numerical and analytical cases outside of the domain. Here, we choose the maximum allowable percent deviation to be 20% in order to define a longer approximate range. In Fig. 10, the numerical and analytical velocities are shown for extreme values of the taper angle, α.

Note that, in Fig. 10a, we show the maximum velocities corresponding to $\alpha = 1^{\circ}$. Since $x_{\text{cons}} = 36.1$, it may be noted that so long as $0 \leq x \leq 36.1$, there is virtually no deviation from the numerical solution. In the range $36.1 \leq x \leq 108.0$, deviations of 1%-2% are observed. For x values greater than 108.0, the percent deviation undergoes a gradual increase until it reaches a maximum of 16.0%.

Figure 10c illustrates the behavior of the numerical and analytical solutions at $\alpha = 9^{\circ}$. Comparing Fig. 10a to Fig. 10c, it is clear that the conservative domain decreases with an increase in taper angle. Hence, the conservative range for 0-to-1% deviation reduces to $0 < x \leq 4$ (here, $x_{\text{cons}} = 4$). For the range $4 < x \leq 22.5$, the percent deviation increases to 20%, which is the maximum allowable error from an engineering perspective. Figure 10b constitutes an intermediate
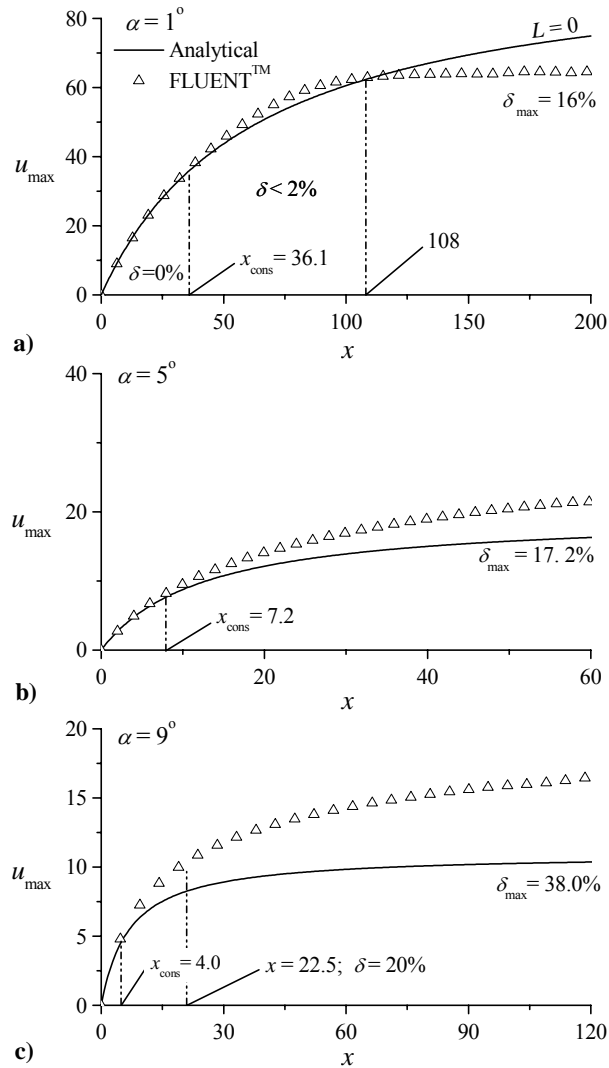
Fig. 10 Numerical and analytical velocities shown at several taper angles. Note that up to x_{cons}, the relative error in the asymptotic expressions is nearly insignificant.

case in which $x_{cons} = 7.2$. Note that even at the end of the domain ($x = 60$), the error remains under 20%.

IX. Conclusions

In this work, we have presented approximate solutions for the mean flowfields in slab rocket motors with tapered walls. Analytical solutions were obtained with the use of two methods: (1) the method of regular perturbations and (2) variation of parameters. The solution resulting from the use of variation of parameters is identical to the leading-order solution

shown earlier. This fact further legitimizes Clayton's approach in which the relationship between the axial pressure gradient and surface vorticity is explored.[16] Although the distance from the axis to the simulated burning surface varies with axial distance, it is assumed constant in the evaluation of key fluid dynamical quantities such as the velocity, vorticity and most notably, the pressure drop.

En route to an expression that characterizes the chamber pressure, multiple operations (differentiations and integrations) were performed with the assumption that the distance from the midsection plane was constant, because its variation was of $O(\sin \alpha)$. This prompted a search for a higher-order correction that would inevitably recover the accuracy lost from this restrictive approximation. In fact, the higher-order corrections were found to compensate for the assumption of axial independence of the half-height of the slab burner. Also, the higher-order corrections recovered the effect of the second-order axial derivative of the stream function as well as the transverse expansion and flow deceleration.

In summary, we have proven that the pressure drop is over-predicted if Taylor's mean flowfield is applied to chambers with tapered walls. A cursory study was attempted by evaluating the momentum thrust along the length of the chamber. The results demonstrated the possibility to over-predict the thrust as well. Our results suggest the need to modify ballistic codes that predict and characterize bulk gas motion in view of taper effects.

Given the methodologies used throughout this work to obtain the desired flowfield, the numerical simulation has been instrumental in substantiating the assumptions posited during the theoretical derivation. Our study confirms the usefulness of adequate numerical models in validating approximate solutions, especially those that are asymptotic in nature.

It may be worth mentioning that accurate matching of both the numerical and analytical solutions requires that the motor parameters are chosen within the specified mean flow asymptotic limits, satisfying the relation given by Eq. (21). One shortcoming in the analytical solution is that it is long, albeit simple to implement and evaluate, and always quicker than CFD. While the leading-order solution can be expressed concisely, it is of marginal accuracy as it can only be applied to motors with short tapered domains and smaller taper angles. Better precision can be achieved when the higher-order corrections are added; in that case the total number of terms required to virtually reproduce the numerical predictions can be anywhere from 6 to 20, depending on the desired accuracy.

References

[1]Culick, F. E. C., "Rotational Axisymmetric Mean Flow and Damping of Acoustic Waves in a Solid Propellant Rocket," *AIAA Journal,* Vol. 4, No. 8, 1966, pp. 1462-1464.

[2]Flandro, G. A., "Energy Balance Analysis of Nonlinear Combustion Instability," *Journal of Propulsion and Power,* Vol. 1, No. 3, 1985, pp. 210-221.

[3]Flandro, G. A., "Effects of Vorticity on Rocket Combustion Stability," *Journal of Propulsion and Power,* Vol. 11, No. 4, 1995, pp. 607-625.

[4]Flandro, G. A., "On Flow Turning," AIAA Paper 95-2530, July 1995.

[5]Flandro, G. A., "Analysis of Nonlinear Combustion Instability," SIAM Minisymposium, March 1998.

[6]Flandro, G. A., and Majdalani, J., "Aeroacoustic Instability in Rockets," *AIAA Journal,* Vol. 41, No. 3, 2003, pp. 485-497.

[7]Flandro, G. A., Majdalani, J., and French, J. C., "Incorporation of Nonlinear Capabilities in the Standard Stability Prediction Program," AIAA Paper 2004-4182, July 2004.

[8]Majdalani, J., and Van Moorhem, W. K., "Improved Time-Dependent Flowfield Solution for Solid Rocket Motors," *AIAA Journal,* Vol. 36, No. 2, 1998, pp. 241-248.

[9]Majdalani, J., and Van Moorhem, W. K., "Laminar Cold-Flow Model for the Internal Gas Dynamics of a Slab Rocket Motor," *Journal of Aerospace Science and Technology,* Vol. 5, No. 3, 2001, pp. 193-207.

[10]Majdalani, J., and Flandro, G. A., "Some Recent Developments in Rocket Core Dynamics," AIAA Paper 2003-5112, July 2003.

[11]Majdalani, J., and Flandro, G. A., "The Oscillatory Pipe Flow with Arbitrary Wall Injection," *Proceedings of the Royal Society, Series A,* Vol. 458, No. 2022, 2002, pp. 1621-1651.

[12]Majdalani, J., and Van Moorhem, W. K., "The Unsteady Boundary Layer in Solid Rocket Motors," AIAA Paper 95-2731, July 1995.

[13]Coats, D. E., and Dunn, S. S., "Solid Performance Program (SPP) Version 7.2 Vav," Software and Engineering Associates, Inc., SEA TR 95-021995.

[14]Coats, D. E., and Dunn, S. S., "Improved Motor Stability Predictions for 3D Grains Using the SPP Code," AIAA Paper 97-33251, July 1997.

[15]Flandro, G. A., "Stability Prediction for Solid Propellant Rocket Motors with High-Speed Mean Flow," Air Force Rocket Propulsion Laboratory, AFRPL-TR-79-98, Edwards AFB, CA, August 1980.

[16]Clayton, C. D., "Flowfields in Solid Rocket Motors with Tapered Bores," AIAA Paper 96-2643, July 1996.

[17]Taylor, G. I., "Fluid Flow in Regions Bounded by Porous Surfaces," *Proceedings of the Royal Society, London, Series A,* Vol. 234, No. 1199, 1956, pp. 456-475.

[18]Yuan, S. W., and Finkelstein, A. B., "Laminar Pipe Flow with Injection and Suction through a Porous Wall," *Transactions of the American Society of Mechanical Engineers: Journal of Applied Mechanics, Series E,* Vol. 78, No. 3, 1956, pp. 719-724.

[19]Yuan, S. W., and Finkelstein, A. B., "Heat Transfer in Laminar Pipe Flow with Uniform Coolant Injection," *Jet Propulsion,* Vol. 28, No. 1, 1958, pp. 178-181.

[20]Terrill, R. M., and Shrestha, G. M., "Laminar Flow through Channels with Porous Walls and with an Applied Transverse Magnetic Field," *Applied Scientific Research,* Vol. 11, 1964, pp. 134-144.

[21]Majdalani, J., Vyas, A. B., and Flandro, G. A., "Higher Mean-Flow Approximation for a Solid Rocket Motor with Radially Regressing Walls," *AIAA Journal,* Vol. 40, No. 9, 2002, pp. 1780-1788.

[22]Zhou, C., and Majdalani, J., "Improved Mean Flow Solution for Slab Rocket Motors with Regressing Walls," *Journal of Propulsion and Power,* Vol. 18, No. 3, 2002, pp. 703-711.

[23]Mu-Kuan, T., and Tong-Miin, L., "Fiber Optic LDV Study of the Non-Uniform, Injection Induced Flow in a 2-D, Divergent, Porous-Walled Channel," *Journal of the Chinese Society of Mechanical Engineers,* Vol. 11, No. 5, 1990, pp. 414-422.

[24]Brown, R. S., Blackner, A. M., Willoughby, P. G., and Dunlap, R., "Coupling between Acoustic Velocity Oscillations and Solid Propellant Combustion," *Journal of Propulsion and Power,* Vol. 2, No. 5, 1986, pp. 428-437.

[25]Brown, R. S., Blackner, A. M., Willoughby, P. G., and Dunlap, R., "Coupling between Velocity Oscillations and Solid Propellant Combustion," Bolling Air Force Base, Final Technical Rept. F49620-81-C-0027, Washington DC, August 1986.

[26]Brown, R. S., Erickson, J. E., and Babcock, W. R., "Measuring the Combustion Response of a Forced Oscillation Method," *AIAA Journal,* Vol. 12, No. 11, 1974, pp. 1502-1510.

[27]Dunlap, R., Blackner, A. M., Waugh, R. C., Brown, R. S., and Willoughby, P. G., "Internal Flow Field Studies in a Simulated Cylindrical Port Rocket Chamber," *Journal of Propulsion and Power,* Vol. 6, No. 6, 1990, pp. 690-704.

[28]Dunlap, R., Willoughby, P. G., and Hermsen, R. W., "Flowfield in the Combustion Chamber of a Solid Propellant Rocket Motor," *AIAA Journal,* Vol. 12, No. 10, 1974, pp. 1440-1445.

[29]Dunlap, R., Sabnis, J. S., Beddini, R. A., Flandro, G. A., Brown, R. S., Gibeling, H. J., Blackner, A. M., Waugh, R. C., and McDonald, H., "Internal Flow Field Investigation," U. S. Air Force Rocket Propulsion Laboratory, TR-85-079, August 1985.

[30]Chu, W.-W., Yang, V., and Majdalani, J., "Premixed Flame Response to Acoustic Waves in a Porous-Walled Chamber with Surface Mass Injection," *Combustion and Flame,* Vol. 133, No. 6129, 2003, pp. 359-370.

[31]Vyas, A. B., Majdalani, J., and Yang, V., "Estimation of the Laminar Premixed Flame Temperature and Velocity in Injection-Driven Combustion Chambers," *Combustion and Flame,* Vol. 133, No. 6129, 2002, pp. 371-374.